Elastic and transport properties of the tailorable multifunctional hierarchical honeycombs

Yongtao Sun [a], Qiang Chen [b], Nicola Pugno [c,d,*]

[a] School of Mechanical Engineering, Tianjin University, Tianjin 300072, PR China
[b] Laboratory of Biomechanics, School of Biological Science and Medical Engineering, Southeast University, Nanjing 210096, PR China
[c] Laboratory of Bio-Inspired & Graphene Nanomechanics, Department of Civil, Environmental and Mechanical Engineering, University of Trento, Trento I-38123, Italy
[d] Center for Materials and Microsystems, Fondazione Bruno Kessler, Via Sommarive 18, 38123 Povo (Trento), Italy

ARTICLE INFO

ABSTRACT

In this paper, we analytically studied the in-plane elastic and transport properties of a peculiar hexagonal honeycomb, i.e., the multifunctional hierarchical honeycomb (MHH). The MHH structure was developed by replacing the solid cell walls of the original regular hexagonal honeycomb (ORHH) with three kinds of equal-mass isotropic honeycomb sub-structures possessing hexagonal, triangular and Kagome lattices. Formulas to calculate the effective in-plane elastic properties and conductivities of the MHH structure at all densities were developed. Results show that the elastic properties of the MHH structure with the hexagonal sub-structure were weakly improved in contrast to those of the ORHH. However, the triangular and Kagome sub-structures result in substantial improvements by one or even three orders of magnitude on Young's and shear moduli of the MHH structure, depending on the cell-wall thickness-to-length ratio of the ORHH. The present theory could be used in designing new tailorable hierarchical honeycomb structures for multifunctional applications.

© 2013 Elsevier Ltd. All rights reserved.

1. Introduction

Low-density cellular materials widely exist in Nature and exhibit fascinating mechanical properties in the aspects of strength, stiffness, toughness, etc. [1–3]. As a typical low-density cellular solid, honeycomb, which is mainly used as cores of light-weight sandwich panel structures [4–7], has been used in many fields, such as aerospace and automotive industries. Apart from its peculiar low-density and mechanical properties, honeycomb also shows other attractive functionalities, e.g., heat transfer, thermal protection, catalysis application and so on. In order to find optimal topologies for different multifunctional applications, varieties of prismatic honeycombs have been developed and studied in recent years.

Regarding the multifunctionality of honeycomb materials, Lu [8] and Gu et al. [9] reported that the regular hexagonal metallic cell, compared with triangular and square cells, provides the highest level of heat dissipation, which is comparable to that of the open-cell metal foams. Combining experimental and numerical methods, Wen et al. [10] revealed that the overall thermal performances of metallic honeycomb structures are superior to other heat sink media, such as metallic foams, lattice-frame materials, 3D Kagome structures and woven textile structures. Employing the topology optimization technique, Hyun and Torquato [11] showed that only the effective conductivity of the regular hexagonal honeycomb tends to the Hashin–Shtrikman (H–S) upper bounds; while for triangular and Kagome honeycombs, both the in-plane effective moduli and conductivity approach the H–S upper bounds [12,13]. Hayes et al. [14] studied the mechanical and thermal properties of linear cellular alloys with square cells, and concluded that the mechanical and heat transfer characteristics of the honeycomb materials outperformed those of the open- and closed-cell metallic foams with comparable relative density. Vaziri and his collaborators [15–25] focused on metallic sandwich panels with different kinds of cellular cores, such as hexagonal honeycombs [15], square honeycombs [16–20], open-cell rhombic dodecahedron cellular structures [21] and pyramidal truss cores [22–25], and explored their multifunctional applications, such as energy absorption [24], sustaining shock loading [16–18] and underwater impulsive loading [19,20]. Besides, Evans et al. [26], Wadley et al. [27] and Wadley [28] reviewed the multifunctionalities and the fabrication technologies of the multifunctional periodic cellular metals with different topological structures.

* Corresponding author. Address: Laboratory of Bio-Inspired & Graphene Nanomechanics, Department of Civil, Environmental and Mechanical Engineering, University of Trento, Trento I-38123, Italy. Tel.: +39 0461 282525; fax: +39 0461 282599.
E-mail address: nicola.pugno@unitn.it (N. Pugno).

Regarding the mechanical properties of honeycomb materials, Wang and McDowell [29] investigated the in-plane stiffness and yield strength of different periodic metallic honeycombs, and showed that the diamond, triangular and Kagome cells have superior in-plane mechanical properties than the hexagonal, rectangular and mixed square/triangular cells. Fleck and Qiu [30] analyzed the damage tolerance property of 2D elastic-brittle isotropic honeycombs and reported that Kagome cells have much higher fracture toughness than those of hexagonal and triangular cells.

Another concept related to honeycomb materials is the introduction of hierarchy. Compared with their single length scale microstructure counterparts, structural hierarchy in natural materials can result in significantly higher stiffness or strength efficiencies (i.e. stiffness- or strength-to-weight ratios), and maintain their flaw-tolerance or energy-absorbing property [31–36]. Therefore, many researchers [37–44] have focused on the mechanical properties of the hierarchical cellular structures. Burgueno et al. [45] studied the hierarchical cellular designs for load-bearing bio-composite beams and plates. Kooistra et al. [46] investigated hierarchical corrugated core sandwich panels and revealed that second-order trusses can have much higher compressive and shear strengths than their equal-mass first-order counterparts when relative densities are less than 5%. Fan et al. [47] studied two-dimensional cellular materials made up of sandwich struts and showed that the relevant mechanical properties of the materials are improved substantially by incorporating structural hierarchy. Inspired by diatom algae which contains nanoporous hierarchical silicified shells, Garcia et al. [48] revealed the toughening mechanism in the superductile wavy silica nanostructures by performing a series of molecular dynamics simulations. Taylor et al. [49] introduced the functionally graded hierarchical honeycombs by performing a set of finite element analyses, and their results suggested that the Young's modulus of the functionally graded hierarchical honeycomb can be 1.75 times that of its equal-mass first-order hexagonal honeycomb if the structure is designed properly. Different from the topology of the common hierarchical honeycomb structures [37,38,43,49], Vaziri's group recently [50] developed a new hierarchical honeycomb structure by replacing every three-edge joint of a regular hexagonal lattice with a smaller hexagon, and showed that the Young's modulus of the hierarchical honeycombs with one level and two levels can be 2.0 and 3.5 times stiffer than their equal-mass regular hexagonal honeycomb, respectively. And more, Chen and Pugno [42–44] explored the buckling behavior of 2D hierarchical honeycombs and Young's modulus and strength of 3D hierarchical foams by considering the surface effect at the bottom level of these structures.

In this paper, along the line, we analytically studied the in-plane elastic moduli and thermal conductivity of a multifunctional hierarchical honeycomb (MHH). The MHH structure is formed by replacing the solid cell walls of an original regular hexagonal honeycomb (ORHH) with three different isotropic honeycomb sub-structures possessing hexagonal, triangular or Kagome lattices. First, we derive the theoretical formulas of the effective elastic moduli of the regular hexagonal honeycombs for all densities. Then, the in-plane Young's, shear and bulk moduli of the three kinds of MHH structures are calculated. Besides, the effective in-plane conductivities of the MHH structures are also formulated through the H–S upper bounds.

2. Effective in-plane elastic moduli of the regular hexagonal honeycombs for all densities

Hyun and Torquato [51] analytically studied the effective in-plane properties of the regular hexagonal honeycomb for all densities via three-point approximations and expressed the effective Young's modulus E_e (Fig. 1b) as

$$\frac{E_e}{E_s} = \frac{\phi(2\zeta-1)(\zeta+\eta-1)}{\{3-2\phi-2(2-\phi)(1-\zeta)+(2-\zeta-\eta)[2\phi(1-\zeta)-1]\}} \quad (1)$$

in which ϕ is the relative density of the hexagonal honeycomb, E_s is the Young's modulus of its constituent solid, ζ and η are the three-point parameters (Fig. 1a). The simulation data of the effective Young's modulus E_e [51] are also provided in Fig. 1b. It is apparent that for the high density case ($\phi \geqslant 0.5$), the prediction by the three-point approximations method matches very well the simulation data, but for the lower density case, it overestimates the results, and in the super low density case, the overestimation is so great that the three-point approximations method is not valid any more.

It is well-known that for the low-density regular hexagonal honeycombs, the Euler beam theory and the Timoshenko beam theory can effectively predict their materials constants. Here, we extend the Euler beam theory and the Timoshenko beam theory to the all relative densities cases and compare the results with the three-point approximations. Under the Euler beam theory, Torquato et al. [52] expressed the effective Young's modulus E_e as:

$$\frac{E_e}{E_s} = \frac{3}{2}\phi^3 \quad (2)$$

And employing the Timoshenko beam theory Gibson and Ashby [3] studied the elastic properties of the low density honeycombs. For the regular hexagonal honeycomb, the effective Young's modulus is given by:

$$\frac{E_e}{E_s} = \frac{4}{\sqrt{3}}\left(\frac{t}{l}\right)^3 \frac{1}{1+(5.4+1.5v_s)(t/l)^2} \quad (3)$$

in which v_s is the Poisson's ratio of its constituent solid and $t/l = \sqrt{3}\left(1-\sqrt{1-\phi}\right)$ is the cell-wall thickness-to-length ratio.

For honeycombs at all densities, the comparison between the Euler beam theory, Timoshenko beam theory, three-point approximations method and the simulation data is plotted in Fig. 1b. We can see that when $\phi \leqslant 0.5$ the result calculated by the Euler beam theory matches very well the simulation data, while the result is well predicted by the three-point approximations method when $\phi > 0.5$. Therefore, the effective Young's modulus of the regular hexagonal honeycombs for all densities can be piecewisely expressed as:

$$\frac{E_e}{E_s} = \begin{cases} \frac{3}{2}\phi^3 & \phi \leqslant 0.5 \\ \frac{\phi(2\zeta-1)(\zeta+\eta-1)}{\{3-2\phi-2(2-\phi)(1-\zeta)+(2-\zeta-\eta)[2\phi(1-\zeta)-1]\}} & \phi > 0.5 \end{cases} \quad (4)$$

Besides, through the three-point approximations method, Hyun and Torquato [51] also derived the effective in-plane bulk modulus k_e of the regular hexagonal honeycomb at all densities:

$$\begin{aligned} \frac{k_e}{k_s} &= \frac{G_s\phi(2\zeta-1)}{k_s(1-\phi)+G_s[1+2\phi(\zeta-1)]} \\ &= \frac{G_s/k_s\phi(2\zeta-1)}{(1-\phi)+G_s/k_s[1+2\phi(\zeta-1)]} \end{aligned} \quad (5)$$
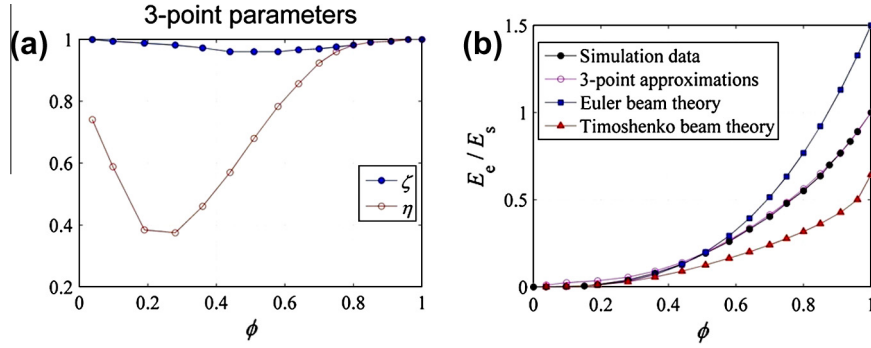
where k_s and G_s are the bulk and shear moduli of the constituent solid, respectively.

Due to the in-plane isotropic properties, k_s, E_s, k_e, G_e and E_e satisfy the following relationships:

$$k_s = \frac{E_s}{2(1-v_s)} \quad (6)$$

$$k_e = \frac{E_e}{2(1-v_e)} \quad (7)$$

$$G_e = \frac{E_e}{2(1+v_e)} \quad (8)$$

Fig. 1. (a) Three-point parameters ζ and η for the regular hexagonal honeycomb [51] vs the relative density ϕ. (b) Effective Young's modulus E_e/E_s of the regular hexagonal honeycomb vs the relative density ϕ predicted by different methods.

in which G_e and ν_e are the effective in-plane shear modulus and Poisson's ratio of the hexagonal honeycombs, respectively. Defining $E_e/E_s = A$ and $k_e/k_s = B$, Eqs. (4)–(8) provide the formula for G_e:

$$\frac{G_e}{E_s} = \frac{AB}{4B - 2A(1 - \nu_s)} \tag{9}$$

Then, the effective Poisson's ratio ν_e of the regular hexagonal honeycombs can be derived through dividing Eq. (6) by Eq. (7):
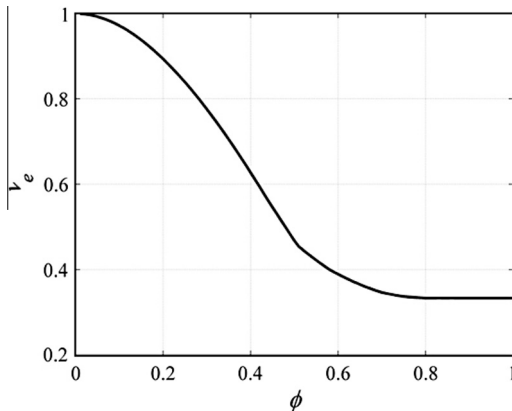
$$\nu_e = 1 - \frac{A}{B}(1 - \nu_s) \tag{10}$$

To verify the expressions of E_e, k_e and G_e, Eq. (10) is depicted in Fig. 2 for the honeycombs at all densities with $\nu_s = 1/3$. Note that in the calculations and following sections, the three-point parameters ζ and η are interpolated from Fig. 1a.

Fig. 2 shows excellent agreement with the existing results [3,53], that is to say, ν_e tends to 1 for the extreme low densities and tends to Poisson's ratio of constituent solid $\nu_s = 1/3$ for the extreme high densities. This implies the validations of Eqs. (4), (5) and (9), which will be employed to study the relevant properties of the MHH. It is worth mentioning that different from the formula in Ref. [3], here Poisson's ratio is not a constant when the relative density is low.

3. MHH with isotropic hexagonal sub-structure

3.1. Basic theory

First of all, we consider the MHH with the isotropic hexagonal lattice sub-structure (Fig. 3). The thicknesses of the ORHH (Fig. 3a) and MHH (Fig. 3b) are denoted by t_0 and t_1, respectively, and their lengths denoted by l_0 are considered to be identical. In particular, one of the MHH cell walls in Fig. 3b is shown in

Fig. 3c, where the cell-wall thickness and length of the hexagonal cells are denoted by t_h and l_h, respectively. The out-of-plane depth is a constant and identical for both structures.

The geometry of Fig. 3c implies:

$$l_0 = nl_h + (n+1)(2l_h) = (3n+2)l_h \tag{11}$$

where n is the number of the solid hexagonal cell walls lying on the middle line of the MHH cell walls (e.g., in Fig. 3c, $n = 8$). Defining $\lambda = l_h/l_0$ as the hierarchical length ratio, rearranging Eq. (11) provides,
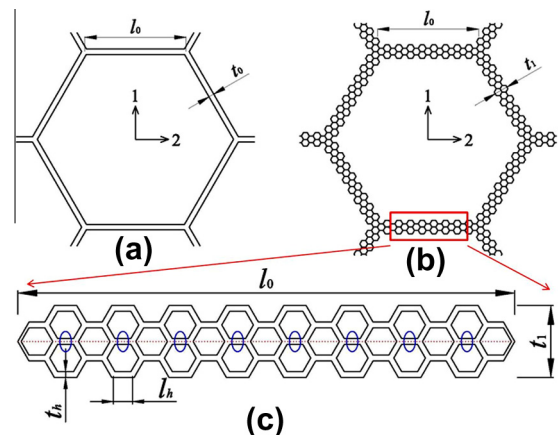
$$\lambda = \frac{1}{3n+2} \tag{12}$$

Then, defining N as the number of hexagonal cells away from the middle line of the MHH cell walls (e.g., in Fig. 3c, $N = 1$), and M the total number of half-thickness hexagonal cells in a MHH cell wall (see Appendix A), then, the relationship between M and N can be expressed as:

$$M = 2N(2n+1) + \frac{n}{3} - 4A_N \tag{13}$$

with $A_N = [(2N+1)(N-1)+1]/6$. After that, basing on the mass equivalence between cell walls of the MHH and the ORHH, we find $t_0 l_0 - \frac{1}{2\sqrt{3}} t_0^2 = 6 \times \frac{1}{2}\left(t_h l_h - \frac{1}{2\sqrt{3}} t_h^2\right) M$, which gives

$$\frac{t_h}{l_h} = \sqrt{3}\left[1 - \sqrt{1 - \frac{2}{3\sqrt{3}\lambda^2 M}\frac{t_0}{l_0}\left(1 - \frac{1}{2\sqrt{3}}\frac{t_0}{l_0}\right)}\right] \tag{14}$$

Besides, a geometrical analysis in Fig. 3c provides N_{max}, the upper bound of N, and t_1, the thickness of the MHH cell walls:

Fig. 2. The effective Poisson's ratio ν_e of the regular hexagonal honeycomb with $\nu_s = 1/3$ vs the relative density ϕ.

Fig. 3. (a) The original regular hexagonal honeycomb (ORHH); (b) the tailorable multifunctional hierarchical honeycomb (MHH) with hexagonal sub-structure; (c) amplification of a hexagonal lattice cell wall in (b) (the cell walls marked by blue circle suggest $n = 8$ and the dash line denotes the middle line of the MHH cell wall).

$$N_{\max} = fl\left[\frac{1}{2\lambda}\right] = fl\left[\frac{3n+2}{2}\right] \tag{15}$$

$$t_1 = \begin{cases} 2N\left(\sqrt{3}l_h\right) + t_h & 1 \leqslant N \leqslant N_{\max} - 1 \\ 2 \times \frac{\sqrt{3}}{2}l_0 & N = N_{\max} \end{cases} \tag{16}$$

where '$fl[\ ]$' is the floor function, which denotes the largest integer not greater than the term in the bracket. Then, rearranging Eq. (16) gives:

$$\frac{t_1}{l_0} = \begin{cases} \left(2\sqrt{3}N + \frac{t_h}{l_h}\right)\lambda & 1 \leqslant N \leqslant N_{\max} - 1 \\ \sqrt{3} & N = N_{\max} \end{cases} \tag{17}$$

On the other hand, Eq. (14) requires $1 - 2/\left(3\sqrt{3}\lambda^2 M\right)t_0/l_0$ $\left[1 - 1/\left(2\sqrt{3}\right)t_0/l_0\right] \geqslant 0$. Considering Eqs. (12) and (13), the inequality provides $N_{\min}$, the lower bound of N:

$$N_{\min} = ce\left[\frac{3n+2 - \sqrt{(3n+2)^2\left[1 - \frac{2}{\sqrt{3}}\frac{t_0}{l_0}\left(1 - \frac{1}{2\sqrt{3}}\frac{t_0}{l_0}\right)\right] + n}}{2}\right] \tag{18}$$

where '$ce[\ ]$' is the ceiling function, which denotes the smallest integer not less than the term in the bracket. Note that Eq. (18) may give $N_{\min} = 0$, in this case $N_{\min} = 1$.

Defining the in-plane Young's, shear and bulk moduli of the ORHH as E_O, G_O and k_O, then, from Eqs. (4), (5) and (9), we find:

$$\frac{E_O}{E_s} = A_O = \begin{cases} \frac{3}{2}\phi_O^3 & \phi_O \leqslant 0.5 \\ \frac{\phi_O(2\zeta_O - 1)(\zeta_O + \eta_O - 1)}{\{3 - 2\phi_O - 2(2-\phi_O)(1-\zeta_O) + (2-\zeta_O-\eta_O)[2\phi_O(1-\zeta_O)-1]\}} & \phi_O > 0.5 \end{cases} \tag{19}$$

$$\frac{k_O}{k_s} = B_O = \frac{G_s/k_s\phi_O(2\zeta_O - 1)}{(1-\phi_O) + G_s/k_s[1 + 2\phi_O(\zeta_O - 1)]} \tag{20}$$

$$\frac{G_O}{E_s} = \frac{A_O B_O}{4B_O - 2A_O(1-v_s)} \tag{21}$$

where,

$$\phi_O = \frac{2}{\sqrt{3}}\frac{t_0}{l_0} - \frac{1}{3}\left(\frac{t_0}{l_0}\right)^2 \left(\frac{t_0}{l_0} \leqslant \sqrt{3}\right) \tag{22}$$

is the relative density of the ORHH.

Besides, Hyun and Torquato [11,51] showed that the effective thermal conductivity of the regular hexagonal honeycomb nearly approaches the H–S upper bounds. Thus, defining the thermal conductivities of the ORHH and the constituent solid as σ_O and σ_s, we approximately obtain:

$$\frac{\sigma_O}{\sigma_s} = \frac{\phi_O}{2 - \phi_O} \tag{23}$$

Note that due to the mathematical analogy, results for the effective thermal conductivity translate immediately into the equivalent results for the effective dielectric constant, electrical conductivity and magnetic permeability.

Similarly, defining the in-plane Young's, shear and bulk moduli and thermal conductivity of the hexagonal sub-structure as E_h, G_h, k_h and σ_h, we obtain:

$$\frac{E_h}{E_s} = A_h = \begin{cases} \frac{3}{2}\phi_h^3 & \phi_h \leqslant 0.5 \\ \frac{\phi_h(2\zeta_h - 1)(\zeta_h + \eta_h - 1)}{\{3 - 2\phi_h - 2(2-\phi_h)(1-\zeta_h) + (2-\zeta_h-\eta_h)[2\phi_h(1-\zeta_h)-1]\}} & \phi_h > 0.5 \end{cases} \tag{24}$$

$$\frac{k_h}{k_s} = B_h = \frac{G_s/k_s\phi_h(2\zeta_h - 1)}{(1-\phi_h) + G_s/k_s[1 + 2\phi_h(\zeta_h - 1)]} \tag{25}$$

$$\frac{G_h}{E_s} = \frac{A_h B_h}{4B_h - 2A_h(1-v_s)} \tag{26}$$

$$\frac{\sigma_h}{\sigma_s} = \frac{\phi_h}{2 - \phi_h} \tag{27}$$

where,

$$\phi_h = \frac{2}{\sqrt{3}}\frac{t_h}{l_h} - \frac{1}{3}\left(\frac{t_h}{l_h}\right)^2 \left(\frac{t_h}{l_h} \leqslant \sqrt{3}\right) \tag{28}$$

is the relative density of the hexagonal sub-structure. Denoting the effective Poisson's ratio of the hexagonal sub-structure by v_h, then, the relation $G_h = E_h/[2(1 + v_h)]$ holds. Then, combining Eqs. (24) and (26) gives,

$$v_h = 1 - \frac{A_h}{B_h}(1 - v_s) \tag{29}$$

Thus,

$$\frac{G_h}{k_h} = \frac{E_h/[2(1+v_h)]}{E_h/[2(1-v_h)]} = \frac{1-v_h}{1+v_h} = \frac{A_h(1-v_s)}{2B_h - A_h(1-v_s)} \tag{30}$$

In the meantime, defining the in-plane Young's, shear and bulk moduli and thermal conductivity of the MHH as E_M, G_M, k_M and σ_M, it is easy to obtain:

$$\frac{E_M}{E_h} = A_M = \begin{cases} \frac{3}{2}\phi_M^3 & \phi_M \leqslant 0.5 \\ \frac{\phi_M(2\zeta_M - 1)(\zeta_M + \eta_M - 1)}{\{3 - 2\phi_M - 2(2-\phi_M)(1-\zeta_M) + (2-\zeta_M-\eta_M)[2\phi_M(1-\zeta_M)-1]\}} & \phi_M > 0.5 \end{cases} \tag{31}$$

$$\frac{k_M}{k_h} = B_M = \frac{G_h/k_h\phi_M(2\zeta_M - 1)}{(1-\phi_M) + G_h/k_h[1 + 2\phi_M(\zeta_M - 1)]} \tag{32}$$

$$\frac{G_M}{E_h} = \frac{A_M B_M}{4B_M - 2A_M(1-v_h)} \tag{33}$$

$$\frac{\sigma_M}{\sigma_h} = \frac{\phi_M}{2 - \phi_M} \tag{34}$$

where,

$$\phi_M = \frac{2}{\sqrt{3}}\frac{t_1}{l_0} - \frac{1}{3}\left(\frac{t_1}{l_0}\right)^2 \left(\frac{t_1}{l_0} \leqslant \sqrt{3}\right) \tag{35}$$

Combining Eqs. (19), (24) and (31) yields the relative Young's modulus E_M/E_O:

$$\frac{E_M}{E_O} = \frac{A_M A_h}{A_O} \tag{36}$$

Similarly, from Eqs. (20), (25) and (32), we can get the relative in-plane bulk modulus k_M/k_O:

$$\frac{k_M}{k_O} = \frac{B_M B_h}{B_O} \tag{37}$$

And from Eqs. (21), (24) and (33), we obtain the relative shear modulus G_M/G_O:

$$\frac{G_M}{G_O} = \frac{A_M B_M A_h}{2B_M - A_M(1-v_h)} \frac{2B_O - A_O(1-v_s)}{A_O B_O} \tag{38}$$

Finally, from Eqs. (23), (27) and (34), we find the relative thermal conductivity σ_M/σ_O:

$$\frac{\sigma_M}{\sigma_O} = \frac{\phi_M \phi_h(2-\phi_O)}{\phi_O(2-\phi_M)(2-\phi_h)} \tag{39}$$

3.2. Effect of N on the relative elastic moduli and thermal conductivity of the MHH with hexagonal sub-structure

To investigate the influence of N on the relative elastic moduli E_M/E_O, G_M/G_O, k_M/k_O and the relative thermal conductivity σ_M/σ_O, here, we discuss the following example with parameters $n = 16$, $\lambda = 1/(3n+2) = 0.02$ and $t_0/l_0 = 0.01$, 0.05, 0.1, 0.2 and 0.3. Then, we can find $N_{\max} = 25$ through Eq. (15), and $N_{\min}$ for each t_0/l_0 through Eq. (18). The results are reported in Figs. 4–6, respectively.

From Fig. 4a and b, we can see that almost for all t_0/l_0 considered, the optimal E_M/E_O and G_M/G_O, which vary between 1 and 2, exist as N increases. Note that the optimal E_M/E_O and G_M/G_O may do not correspond to the same N. The reason is that E_O/E_s and
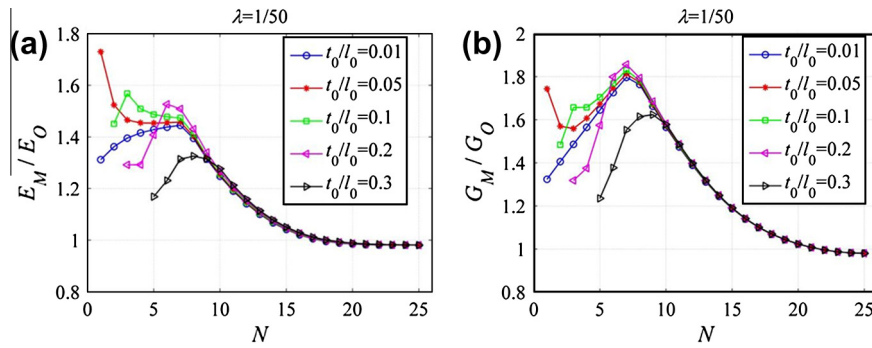
Fig. 4. (a) The relative Young's modulus E_M/E_O vs N for different t_0/l_0. (b) The relative shear modulus G_M/G_O vs N for different t_0/l_0.
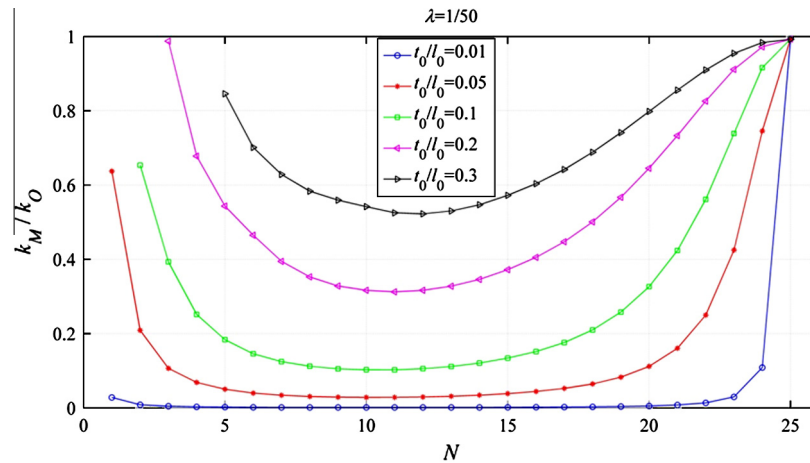

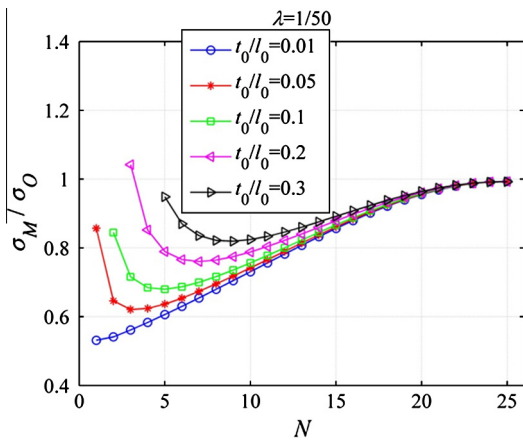**Fig. 5.** The relative bulk modulus G_M/G_O vs N for different t_0/l_0.

Fig. 6. The relative thermal conductivity G_M/G_O vs N for different t_0/l_0.

E_M/E_h depend on Poisson's ratios v_s and v_h but G_O/G_s and G_M/G_h do not [51].

Figs. 5 and 6 show that the relative bulk modulus k_M/k_O and the relative thermal conductivity σ_M/σ_O increase with the increase of t_0/l_0, but in general, they are less than one. This implies that the effective bulk modulus and thermal conductivity of the MHH with regular hexagonal sub-structure are less than those of the ORHH structure. Of particular interest, there is the lowest value for the thermal conductivity, and this could be used to design low heat conductivity materials with the optimal topology.

3.3. The effects of t_0/l_0-the cell-wall thickness-to-length ratio of the ORHH

To investigate the effects of the cell-wall thickness-to-length ratio t_0/l_0 of the ORHH on the relative elastic moduli and thermal conductivity of the MHH structure, again, we use the above example given in Section 3.2. We maintain $n = 16$, $\lambda = 0.02$ but vary t_0/l_0 from 0.01 to 0.5 with an increment of 0.01. In fact, under the same N, the value of G_M/G_O is slightly greater than E_M/E_O (Fig. 4), so here we only consider the relative Young's modulus E_M/E_O influenced by t_0/l_0. Regarding σ_M/σ_O and k_M/k_O, the discussions on them will not be treated in this section, since their values are less than one (Figs. 5 and 6), which shows the inferior properties of the MHH to those of the ORHH.

Finally, the maximum E_M/E_O influenced by t_0/l_0 is reported in Fig. 7. We can see that the maximum E_M/E_O increases before t_0/l_0 reaches 0.07 but after that it decreases. In other words, the optimal E_M/E_O of the MHH with hexagonal sub-structure exists at $t_0/l_0 = 0.07$, of which the value approximately equals 2. The result is comparable to the finite element result given by Taylor et al. [49].

4. MHH with triangular sub-structure

4.1. Basic theory

In this section, we obtain the second topology of the MHH by substituting the ORHH cell walls with the equal-mass isotropic triangular sub-structure, see Fig. 8. As defined in Section 3, the hierarchical length ratio is expressed as
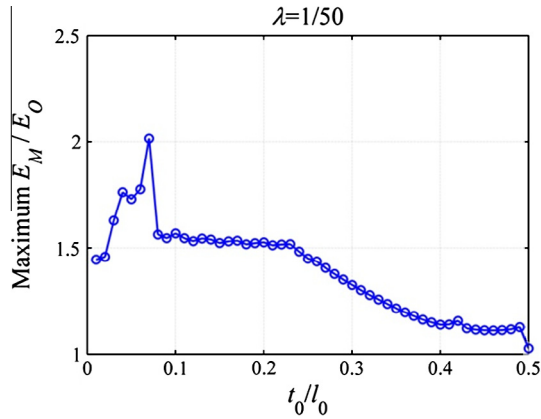
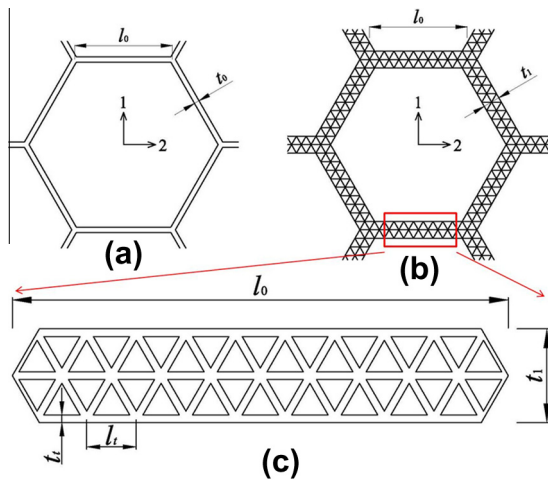**Fig. 7.** The maximum E_M/E_O vs t_0/l_0.

Fig. 8. Schematics of (a) the ORHH; (b) the tailorable MHH with triangular sub-structure; and (c) amplification of a triangular lattice cell wall in (b).

$$\lambda = \frac{l_t}{l_0} = \frac{1}{n} (n \geqslant 1) \tag{40}$$

where n is the number of solid triangular lattice cell walls lying on the middle line of the MHH cell walls. From Fig. 8c, according to the equal-mass principle, we can find $t_0 l_0 - \frac{1}{2\sqrt{3}} t_0^2 = 3 \times \frac{1}{2} \left(t_t l_t - \frac{\sqrt{3}}{2} t_t^2 \right) M$, which gives

$$\frac{t_t}{l_t} = \frac{1}{\sqrt{3}} \left[1 - \sqrt{1 - \frac{4\sqrt{3}}{3\lambda^2 M} \frac{t_0}{l_0} \left(1 - \frac{1}{2\sqrt{3}} \frac{t_0}{l_0} \right)} \right] \tag{41}$$

where M is the total number of half thickness triangular lattice cells in a MHH cell wall and it has the following relationship with n and N (see Appendix B):

$$M = 2N(2n - N) + \frac{2}{3}(n - N)(1 \leqslant N \leqslant n) \tag{42}$$

in which N is the number of triangular lattice cells away from the middle line of the MHH cell walls. Similar to that in Section 3, a geometrical analysis in Fig. 8c provides N_{max}, the upper bound of N, and t_1, the thickness of the MHH cell walls:

$$N_{max} = n \tag{43}$$

$$t_1 = \begin{cases} 2N\left(\frac{\sqrt{3}}{2} l_t\right) + t_t & 1 \leqslant N \leqslant N_{max} - 1 \\ 2 \times \frac{\sqrt{3}}{2} l_0 & N = N_{max} \end{cases} \tag{44}$$

Then, rearranging Eq. (44) gives,

$$\frac{t_1}{l_0} = \begin{cases} \left(\sqrt{3}N + \frac{t_t}{l_t} \right)\lambda & 1 \leqslant N \leqslant N_{max} - 1 \\ \sqrt{3} & N = N_{max} \end{cases} \tag{45}$$

On the other hand, Eq. (41), requires $1 - 4\sqrt{3}/(3\lambda^2 M)t_0/l_0 \left[1 - 1/\left(2\sqrt{3}\right)t_0/l_0 \right] \geqslant 0$. Then, employing Eqs. (40) and (42), the inequality gives N_{min}, the lower bound of N:

$$N_{min} = ce \left[\frac{6n - 1 - \sqrt{(6n-1)^2 - 12n\left[2\sqrt{3}n\frac{t_0}{l_0}\left(1 - \frac{1}{2\sqrt{3}}\frac{t_0}{l_0}\right) - 1\right]}}{6} \right] \tag{46}$$

Note that Eq. (46) may give $N_{min} = 0$, in this case $N_{min} = 1$.

Like the discussion in Section 3, we would like to analyze the effective elastic moduli and thermal conductivity of the triangular lattice sub-structure. As mentioned in the introduction, Hyun and Torquato [11] showed that for triangular and Kagome honeycombs, both the in-plane effective moduli and conductivity approach the H–S upper bounds [12,13]. So, we approximately use the H–S upper bounds to calculate the effective elastic moduli and thermal conductivity of the triangular lattice sub-structure. Defining the in-plane Young's, shear and bulk moduli and thermal conductivity of the triangular sub-structure as E_t, G_t, k_t and σ_t, we obtain:

$$\frac{E_t}{E_s} = A_t = \frac{\phi_t}{3 - 2\phi_t} \tag{47}$$

$$\frac{k_t}{k_s} = B_t = \frac{\phi_t G_s/k_s}{1 - \phi_t + G_s/k_s} \tag{48}$$

$$\frac{G_t}{E_s} = C_t = \frac{1}{2(1 + v_s)} \frac{\phi_t}{(1 - \phi_t)(1 + 2G_s/k_s) + 1} \tag{49}$$

$$\frac{\sigma_t}{\sigma_s} = \frac{\phi_t}{2 - \phi_t} \tag{50}$$

where,

$$\phi_t = 2\sqrt{3}\frac{t_t}{l_t} - 3\left(\frac{t_t}{l_t}\right)^2 \left(\frac{t_t}{l_t} \leqslant \frac{1}{\sqrt{3}}\right) \tag{51}$$

is the relative density of the triangular sub-structure. Denoting the effective Poisson's ratio of the triangular sub-structure by v_t, the relation $G_t = E_t/[2(1 + v_t)]$ holds. Then, combining Eqs. (47) and (49) gives,

$$v_t = \frac{1}{2}\frac{A_t}{C_t} - 1 \tag{52}$$

Thus,

$$\frac{G_t}{k_t} = \frac{E_t/[2(1 + v_t)]}{E_t/[2(1 - v_t)]} = \frac{1 - v_t}{1 + v_t} = 4\frac{C_t}{A_t} - 1 \tag{53}$$

Defining the in-plane Young's, shear and bulk moduli and thermal conductivity of the MHH with triangular sub-structure as E_M, G_M, k_M and σ_M, we have:

$$\frac{E_M}{E_t} = A_M = \begin{cases} \frac{3}{2}\phi_M^3 & \phi_M \leqslant 0.5 \\ \frac{\phi_M(2\zeta_M - 1)(\zeta_M + \eta_M - 1)}{\{3 - 2\phi_M - 2(2 - \phi_M)(1 - \zeta_M) + (2 - \zeta_M - \eta_M)[2\phi_M(1 - \zeta_M) - 1]\}} & \phi_M > 0.5 \end{cases} \tag{54}$$

$$\frac{k_M}{k_t} = B_M = \frac{G_t/k_t \phi_M(2\zeta_M - 1)}{(1 - \phi_M) + G_t/k_t[1 + 2\phi_M(\zeta_M - 1)]} \tag{55}$$

$$\frac{G_M}{E_t} = \frac{A_M B_M}{4B_M - 2A_M(1 - v_t)} \tag{56}$$

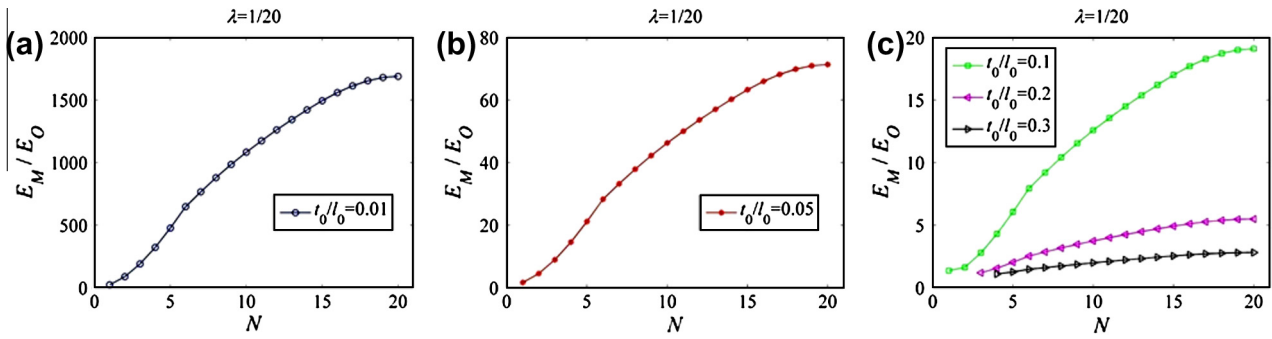$$\frac{\sigma_M}{\sigma_t} = \frac{\phi_M}{2 - \phi_M} \tag{57}$$

where,

Fig. 9. The relative Young's modulus E_M/E_O vs N for different t_0/l_0: (a) $t_0/l_0 = 0.01$; (b) $t_0/l_0 = 0.05$; and (c) $t_0/l_0 = 0.1, 0.2, 0.3$.

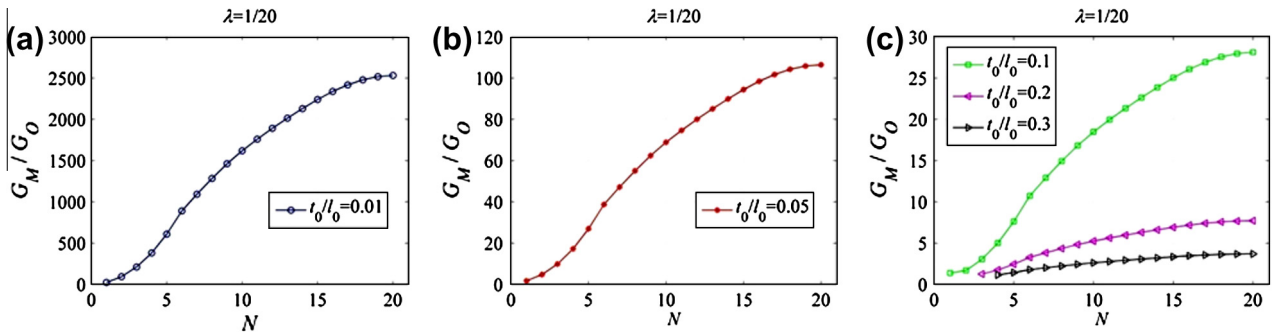**Fig. 10.** The relative Young's modulus G_M/G_O vs N for different t_0/l_0: (a) $t_0/l_0 = 0.01$; (b) $t_0/l_0 = 0.05$; (c) $t_0/l_0 = 0.1, 0.2, 0.3$.

$$\phi_M = \frac{2}{\sqrt{3}} \frac{t_1}{l_0} - \frac{1}{3}\left(\frac{t_1}{l_0}\right)^2 \left(\frac{t_1}{l_0} \leqslant \sqrt{3}\right) \tag{58}$$

and ζ_M and η_M, interpolated from Fig. 1a, are the three-point parameters corresponding to ϕ_M.

Combining Eqs. (19), (47) and (54) gives the relative Young's modulus E_M/E_O:

$$\frac{E_M}{E_O} = \frac{A_M A_t}{A_O} \tag{59}$$

Similarly, from Eqs. (20), (48) and (55), we can find the relative bulk modulus k_M/k_O:

$$\frac{k_M}{k_O} = \frac{B_M B_t}{B_O} \tag{60}$$

And from Eqs. (21), (47) and (56), we obtain the relative shear modulus G_M/G_O:

$$\frac{G_M}{G_O} = \frac{A_M B_M A_t}{2B_M - A_M(1 - v_t)} \frac{2B_O - A_O(1 - v_s)}{A_O B_O} \tag{61}$$

Finally, from Eqs. (23), (50) and (57), the relative thermal conductivity σ_M/σ_O is derived:

$$\frac{\sigma_M}{\sigma_O} = \frac{\phi_M \phi_t (2 - \phi_O)}{\phi_O(2 - \phi_M)(2 - \phi_t)} \tag{62}$$

4.2. Effects of N on the relative elastic moduli and thermal conductivity of the MHH with triangular sub-structure

As discussed in Section 3, the influence of N on the effective elastic moduli and thermal conductivity of the MHH with triangular sub-structure are studied, here we consider the second example with parameters $n = 20$, $\lambda = 1/n = 0.05$, $t_0/l_0 = 0.01, 0.05, 0.1, 0.2$ and 0.3. Then, we immediately obtain $N_{max} = 20$ by Eq. (23) and the
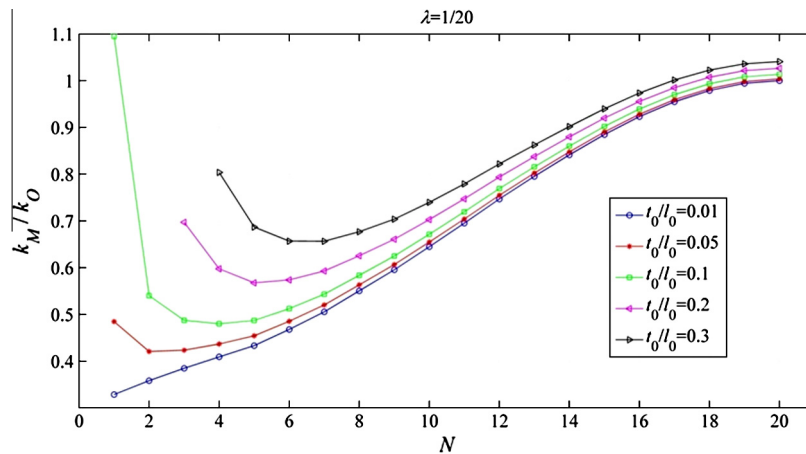

Fig. 11. The relative bulk modulus k_M/k_O vs N for different t_0/l_0.

lower bound $N_{\min}$ for each t_0/l_0 by Eq. (46). The relative elastic moduli E_M/E_O, G_M/G_O, k_M/k_O and the relative thermal conductivity σ_M/σ_O vs N are reported in Figs. 9–12, respectively.

Figs. 9 and 10 show that the relative Young's modulus E_M/E_O and the relative shear modulus G_M/G_O increase with the increase of N, and the thickness-to-length ratio t_0/l_0 has a strong influence on them. With respect to its equal-mass ORHH, the enhancements of the relative Young's and shear moduli of the MHH can be one order (Figs. 9c and 10c) or even three orders of magnitude (Figs. 9a and 10a). Although the enhancement on Young's modulus of the MHH decreases with the increase of t_0/l_0, for a smaller t_0/l_0 (less than 0.3), its stiffening effect (Figs. 9 and 10) by the triangular sub-structure is much larger than that of the hexagonal counterpart (Fig. 4a and b).

The relative bulk modulus k_M/k_O and the relative thermal conductivity σ_M/σ_O shown in Figs. 11 and 12 have similar trends to those of the MHH with the hexagonal sub-structure reported in Section 3.2. Thus, the discussion is omitted here.

5. MHH with isotropic Kagome sub-structure

5.1. Basic theory

Kagome honeycomb has been revealed to have pronounced fracture toughness [30] and better thermal–mechanical performance than the triangular honeycomb [54]. Therefore, in this section, we will consider the third topology of the MHH, namely, substituting the ORHH cell walls with their equal-mass Kagome sub-structure (Fig. 13), and study its effective elastic moduli and thermal conductivity. In this case, the hierarchical length ratio is expressed as:

$$\lambda = \frac{l_k}{l_0} = \frac{1}{n} \quad n = 4, 6, 8, 10 \ldots \tag{63}$$

where l_k is the side length of triangles in Kagome cells and n is the number of sides of the effective triangles on the middle line of the MHH cell walls. Again, the equal-mass principle provides $t_0 l_0 - \frac{1}{2\sqrt{3}} t_0^2 = 3 \times \left(t_k l_k - \frac{\sqrt{3}}{2} t_k^2 \right) M$, and t_k/l_k is derived as:

$$\frac{t_k}{l_k} = \frac{1}{\sqrt{3}} \left[1 - \sqrt{1 - \frac{2\sqrt{3}}{3\lambda^2 M} \frac{t_0}{l_0} \left(1 - \frac{1}{2\sqrt{3}} \frac{t_0}{l_0} \right)} \right] \tag{64}$$

where M is the total number of triangles in a MHH cell wall, and it is expressed with n and N as (see Appendix C):

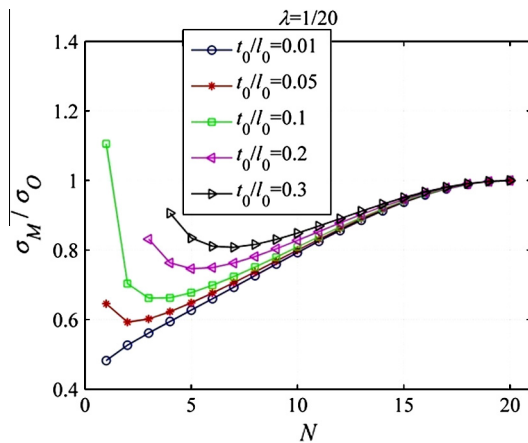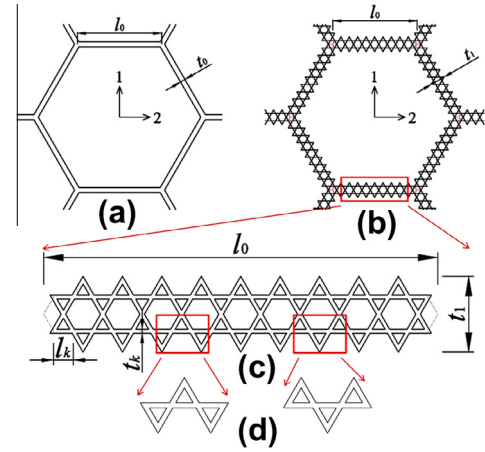$$M = 2N(n - N) \left(1 \leqslant N \leqslant \frac{n}{2} \right) \tag{65}$$

Fig. 13. Schematics of (a) the ORHH; (b) the tailorable MHH with Kagome substructure (in this paper the red dashline is for the convenience of linear dimension); (c) amplication of a Kagome sub-structure cell wall in (b); and (d) the representative cells for the Kagome honeycomb.

in which N is the number of the Kagome representative cells away from the middle line of the MHH cell walls (e.g., in Fig. 13c, $N = 1$). Similar to those in Sections 3 and 4, a geometrical analysis in Fig. 13c provides $N_{\max}$, the upper bound of N, and t_1, the thickness of the MHH cell walls:

$$N_{\max} = \frac{n}{2} \tag{66}$$

$$t_1 = \begin{cases} 2N\left(\sqrt{3}l_k\right) + 2t_k & 1 \leqslant N \leqslant N_{\max} - 1 \\ 2 \times \frac{\sqrt{3}}{2} l_0 & N = N_{\max} \end{cases} \tag{67}$$

Then, rearranging Eq. (67) gives

$$\frac{t_1}{l_0} = \begin{cases} 2\left(\sqrt{3}N + \frac{t_k}{l_k}\right)\lambda & 1 \leqslant N \leqslant N_{\max} - 1 \\ \sqrt{3} & N = N_{\max} \end{cases} \tag{68}$$

Again, Eq. (64) requires $1 - 2\sqrt{3}/(3\lambda^2 M)t_0/l_0\left[1 - 1/\left(2\sqrt{3}\right)t_0/l_0\right] \geqslant 0$. In conjunction with Eqs. (63) and (65), the inequality produces $N_{\min}$, the lower bound of N:

$$N_{\min} = ce\left[\frac{n - n\sqrt{1 - \frac{4\sqrt{3}}{3}\frac{t_0}{l_0}\left(1 - \frac{1}{2\sqrt{3}}\frac{t_0}{l_0}\right)}}{2}\right] \tag{69}$$

Also, when $N_{\min} = 0$, Eq. (69) provides $N_{\min} = 1$.

Here, the H–S upper bounds is again employed to analyze the effective elastic moduli and thermal conductivity of the Kagome lattice sub-structure. Defining the in-plane Young's, shear and bulk moduli and thermal conductivity of the Kagome sub-structure as E_k, G_k, k_k and σ_k, respectively, we obtain:

$$\frac{E_k}{E_s} = A_k = \frac{\phi_k}{3 - 2\phi_k} \tag{70}$$

$$\frac{k_k}{k_s} = B_k = \frac{\phi_k G_s/k_s}{1 - \phi_k + G_s/k_s} \tag{71}$$

$$\frac{G_k}{E_s} = C_k = \frac{1}{2(1 + v_s)}\frac{\phi_k}{(1 - \phi_k)(1 + 2G_s/k_s) + 1} \tag{72}$$

$$\frac{\sigma_k}{\sigma_s} = \frac{\phi_k}{2 - \phi_k} \tag{73}$$

where,

$$\phi_k = \sqrt{3}\frac{t_k}{l_k} - \left(\frac{t_k}{l_k}\right)^2 \left(\frac{t_k}{l_k} \leqslant \frac{1}{\sqrt{3}}\right) \tag{74}$$

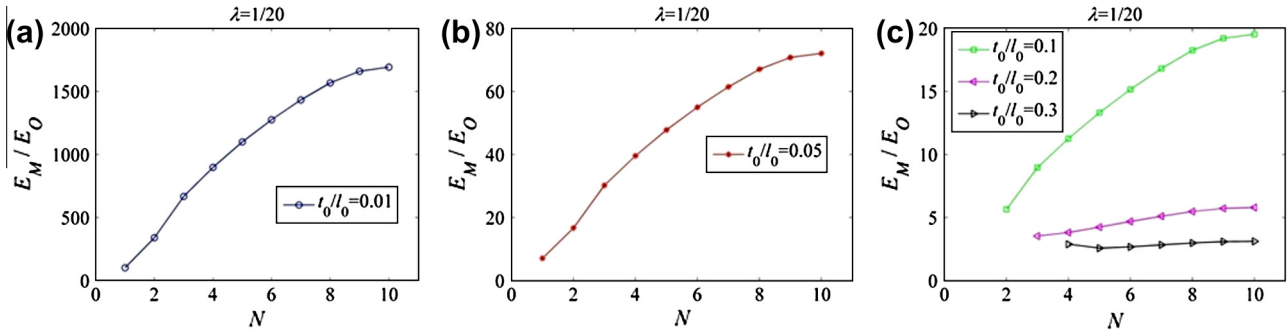Fig. 12. The relative thermal conductivity σ_M/σ_O vs N for different t_0/l_0.

Fig. 14. The relative Young's modulus E_M/E_O vs N for different t_0/l_0: (a) $t_0/l_0 = 0.01$; (b) $t_0/l_0 = 0.05$; and (c) $t_0/l_0 = 0.1, 0.2, 0.3$.
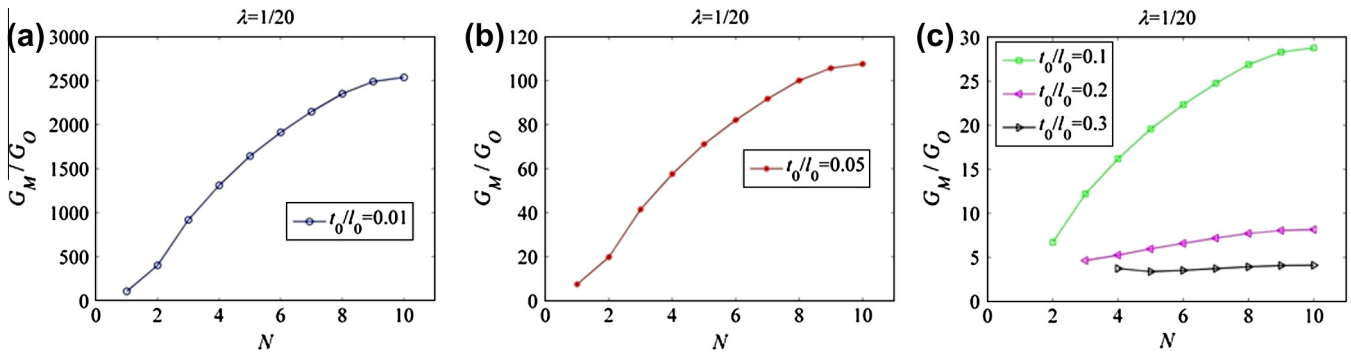

Fig. 15. The relative Young's modulus G_M/G_O vs N for different t_0/l_0: (a) $t_0/l_0 = 0.01$; (b) $t_0/l_0 = 0.05$; and (c) $t_0/l_0 = 0.1, 0.2, 0.3$.
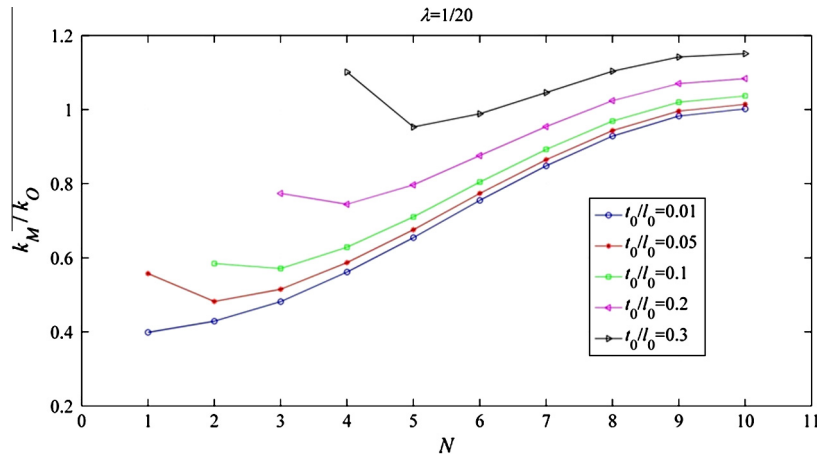

Fig. 16. The relative bulk modulus k_M/k_O vs N for different t_0/l_0.

is the relative density of the Kagome sub-structure. Denoting the effective Poisson's ratio of the Kagome sub-structure by v_k, employing $G_k = E_k/[2(1 + v_k)]$ and combining Eqs. (70) and (72) give

$$v_k = \frac{1}{2}\frac{A_k}{C_k} - 1 \tag{75}$$

Thus,

$$\frac{G_k}{k_k} = \frac{E_k/[2(1 + v_k)]}{E_k/[2(1 - v_k)]} = \frac{1 - v_k}{1 + v_k} = 4\frac{C_k}{A_k} - 1 \tag{76}$$

Again, defining the in-plane Young's, shear and bulk moduli and thermal conductivity of the MHH with Kagome sub-structure as E_M, G_M, k_M and σ_M, we have:

$$\frac{E_M}{E_k} = A_M = \begin{cases} \frac{3}{2}\phi_M^3 & \phi_M \leqslant 0.5 \\ \frac{\phi_M(2\zeta_M-1)(\zeta_M+\eta_M-1)}{\{3-2\phi_M-2(2-\phi_M)(1-\zeta_M)+(2-\zeta_M-\eta_M)[2\phi_M(1-\zeta_M)-1]\}} & \phi_M > 0.5 \end{cases} \tag{77}$$

$$\frac{k_M}{k_k} = B_M = \frac{G_k/k_k\phi_M(2\zeta_M-1)}{(1-\phi_M)+G_k/k_k[1+2\phi_M(\zeta_M-1)]} \tag{78}$$

$$\frac{G_M}{E_k} = \frac{A_M B_M}{4B_M - 2A_M(1-v_k)} \tag{79}$$

$$\frac{\sigma_M}{\sigma_k} = \frac{\phi_M}{2-\phi_M} \tag{80}$$

where,

$$\phi_M = \frac{2}{\sqrt{3}}\frac{t_1}{l_0} - \frac{1}{3}\left(\frac{t_1}{l_0}\right)^2 \left(\frac{t_1}{l_0} \leqslant \sqrt{3}\right) \tag{81}$$

Combining Eqs. (19), (70) and (77) gives the relative Young's modulus E_M/E_O:

$$\frac{E_M}{E_O} = \frac{A_M A_k}{A_O} \qquad (82)$$

Similarly, from Eqs. (20), (71) and (78) we can get the relative bulk modulus k_M/k_O:

$$\frac{k_M}{k_O} = \frac{B_M B_k}{B_O} \qquad (83)$$

And from Eqs. (21), (70) and (79) we obtain the relative shear modulus G_M/G_O:

$$\frac{G_M}{G_O} = \frac{A_M B_M A_k}{2B_M - A_M(1 - v_k)} \frac{2B_O - A_O(1 - v_s)}{A_O B_O} \qquad (84)$$

Finally, from Eqs. (23), (50) and (57), we find the relative thermal conductivity σ_M/σ_O:

$$\frac{\sigma_M}{\sigma_O} = \frac{\phi_M \phi_k (2 - \phi_O)}{\phi_O (2 - \phi_M)(2 - \phi_k)} \qquad (85)$$

5.2. Effects of N on the relative elastic moduli and thermal conductivity of the MHH with Kagome sub-structure

In this section, we consider the third example with parameters $n = 20$, $\lambda = 1/n = 0.05$, $t_0/l_0 = 0.01$, 0.05, 0.1, 0.2 and 0.3. Then, Eq. (66) provides $N_{max} = 10$ and Eq. (69) the lower bound N_{min} for each t_0/l_0. The results of the relative elastic moduli E_M/E_O, G_M/G_O, k_M/k_O and the relative thermal conductivity σ_M/σ_O vs N are shown in Figs. 14–17, respectively.

Comparing Figs. 14 and 15 with Figs. 9 and 10, we can see that Young's and shear moduli of the MHH with Kagome sub-structure are similar to those of the MHH with triangular sub-structure, so the discussion can be referred to the Section 4.

However, it is worth to say that, different from the MHH with hexagonal and triangular sub-structures, the relative bulk modulus k_M/k_O and the relative thermal conductivity σ_M/σ_O of the MHH with Kagome sub-structure become greater than one with the increase of t_0/l_0 (Figs. 16 and 17). This is to say, when t_0/l_0 is great enough, the effective bulk modulus and thermal conductivity of the MHH with Kagome sub-structure could be beyond those of the ORHH structures.

6. Comparisons of hexagonal, triangular and Kagome sub-structures

Comparing the examples discussed in Sections 3–5, it is apparent that for an ORHH, the in-plane stiffness enhancements of the
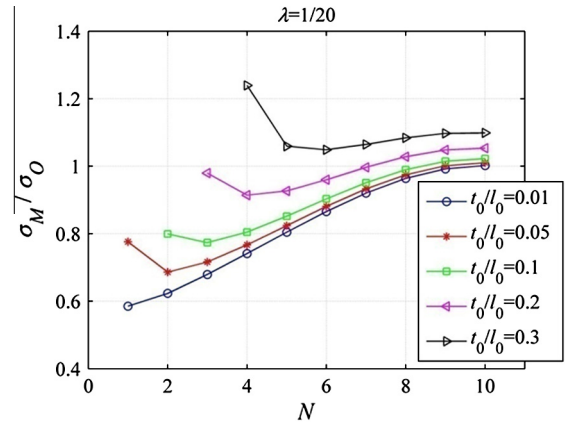

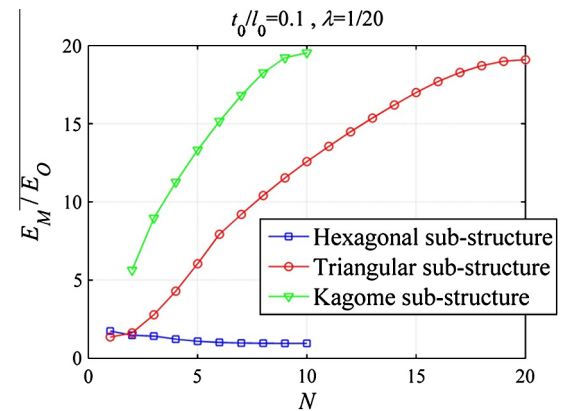**Fig. 17.** The relative thermal conductivity σ_M/σ_O vs N for different t_0/l_0.

Fig. 18. The relative Young's modulus E_M/E_O vs N for different sub-structures with the same parameters $t_0/l_0 = 0.1$ and $\lambda = 1/20$.

MHH with triangular and Kagome sub-structures could be much greater than that with the hexagonal sub-structure. This is illustrated by the fourth examples with the parameters $t_0/l_0 = 0.1$ and $\lambda = 1/20$ and the result is plotted in Fig. 18, in which the relative Young's modulus E_M/E_O versus N for the MHH with the above three sub-structures are reported. Interestingly, we find that the relative Young's moduli of the MHH with triangular and Kagome sub-structures increase as N increases in contrast to that with hexagonal sub-structure. And more, Young's modulus of the MHH with Kagome sub-structure is improved most with respect to the ORHH.
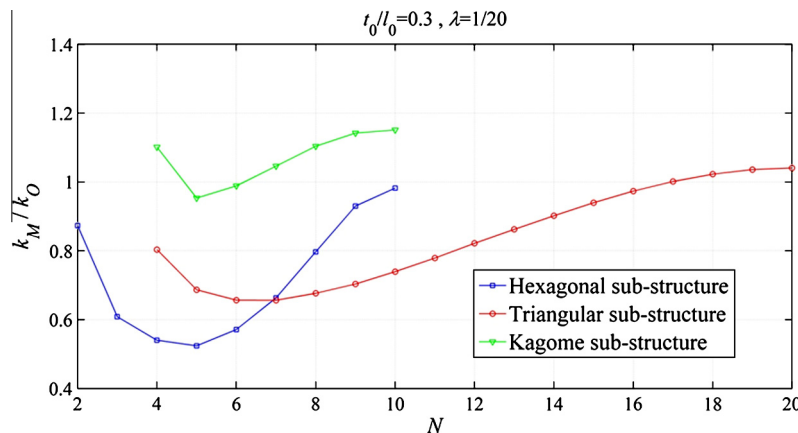

Fig. 19. The relative bulk modulus k_M/k_O vs N for different sub-structures with the same parameters $t_0/l_0 = 0.3$ and $\lambda = 1/20$.
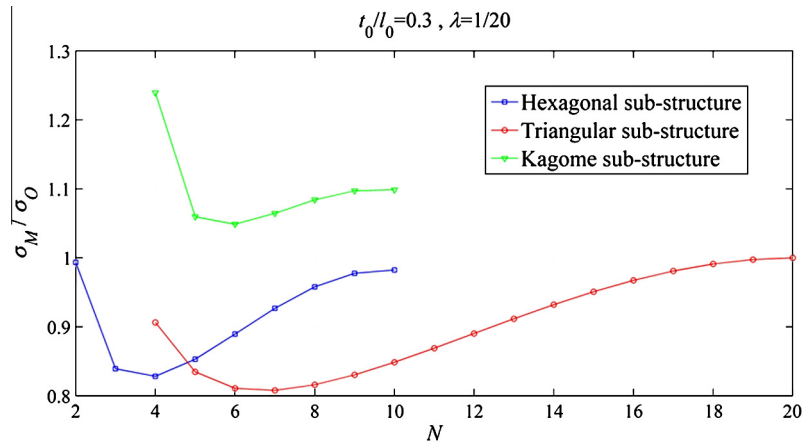
Fig. 20. The relative thermal conductivity σ_M/σ_O vs N for different sub-structures with the same parameters $t_0/l_0 = 0.3$ and $\lambda = 1/20$.

For the comparisons on bulk modulus and thermal conductivity of the three MHHs, the parameters $t_0/l_0 = 0.3$ and $\lambda = 1/20$ are employed, and the results are depicted in Figs. 19 and 20, respectively. From the two figures, we can say that the MHH with Kagome sub-structure is the optimal structure to design the bulk modulus and thermal conductivity of the multifunctional regular hexagonal honeycomb.

7. Conclusions

In this paper, we have studied the in-plane elastic and transport properties of the MHH, which is formed by replacing the ORHH solid cell walls with three types of equal-mass isotropic honeycomb sub-structures. The analytical results show that with the hexagonal sub-structure it is difficult to greatly increase Young's and shear moduli of the MHH. Whereas, triangular and Kagome sub-structures share a similar improvement on the MHH's Young's and shear moduli, and the improvement is substantial, from one order to three orders of magnitude depending on the cell-wall thickness-to-length ratio t_0/l_0 of the ORHH. Meanwhile, if t_0/l_0 is great enough, the effective bulk modulus and transport ability of the MHH with Kagome sub-structure can exceed those of the ORHH structure. These interesting findings show a possibility to design hierarchical honeycombs for multifunctional applications, e.g., the metallic MHH can be used as the core of light weight sandwich panels in electronic packages and airborne devices, where both the structural and thermal characteristics are desirable.

Appendix A. MHH cell wall with hexagonal sub-structures

Fig. A.1 shows the representative cell walls of the MHH with regular hexagonal sub-structures in Fig. 3b. The mass of the sub-structure is distributed uniformly among the half-thickness hexagonal sub-structure cells within the blue hexagon.
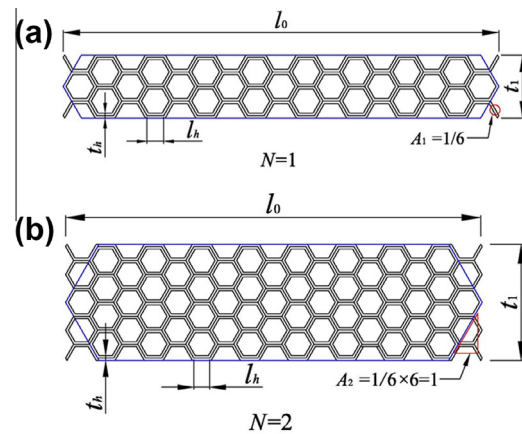

Fig. A.1. Schematics of MHH cell walls in Fig. 1b: (a) $N = 1$ and (b) $N = 2$.

From Fig. A.1 we can see that the number of the half-thickness hexagonal sub-structure cells M can be determined by n and N as the following form:

$$M = 2N[n + (n+1)] + \frac{1}{6}(2n) - 4A_N$$
$$= 2N(2n+1) + \frac{n}{3} - 4A_N \tag{A.1}$$

in which $A_1 = 1/6$ and $A_2 = 1$.

Here, A_N depends on N, we find it generally expressed as:

$$A_N = \frac{(2N+1)(N-1)+1}{6}(N \geqslant 1) \tag{A.2}$$

Appendix B. MHH cell wall with triangular sub-structures

Fig. B.1 schematically shows the cell wall of the MHH with triangular sub-structures (Fig. 8b). The hierarchical length ratio is $\lambda = 1/n$. M is the total number of the half-thickness triangular cells in one sub-structure cell wall. It is easily to get the following relation between M, N and n:

$$N = 1 : M = 2(2n \times 1 - 1) + \frac{2}{3}(n-1)$$
$$N = 2 : M = 2(2n \times 2 - 1 - 1 - 2) + \frac{2}{3}(n-2) \tag{B.1}$$
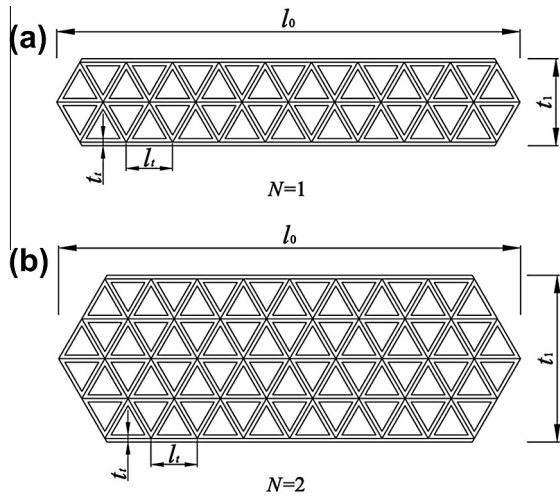$$N = 3 : M = 2(2n \times 3 - 1 - 1 - 2 - 2 - 3) + \frac{2}{3}(n-3)$$

Fig. B.1. Schematics for the representative cell walls of the MHH with triangular sub-structures: (a) $N = 1$ and (b) $N = 2$.
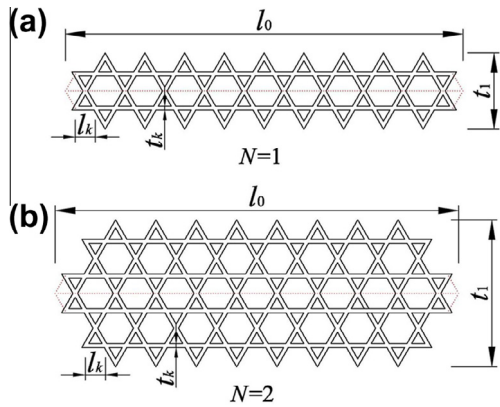

Fig. C.1. Schematics for the representative cell walls of the MHH with Kagome sub-structures: (a) $N = 1$ and (b) $N = 2$.

Then, by inductive method, we find:

$$M = 2(2n \times N - B_N) + \frac{2}{3}(n - N)\,1 \leqslant N \leqslant n \quad (B.2)$$

with

$$B_N = N^2 \quad (B.3)$$

Substituting Eq. (B.3) into Eq. (B.2) gives:

$$M = 2N(2n - N) + \frac{2}{3}(n - N)(1 \leqslant N \leqslant n) \quad (B.4)$$

Appendix C. MHH cell wall with Kagome sub-structures

Fig. C.1 schematically shows the cell wall of the MHH with Kagome sub-structures. The hierarchical length ratio is $\lambda = 1/n$. M is the total number of the triangular cells included in one Kagome sub-structure cell wall. Then, the relationship between M, N and n are expressed as:

$$
\begin{aligned}
N &= 1 : M = 2[(n - 1) - 0] \\
N &= 2 : M = 2[2(n - 1) - 2] \\
N &= 3 : M = 2[3(n - 1) - 2 - 4]
\end{aligned}
\quad (C.1)
$$

Likewise, we find:

$$M = 2[N(n - 1) - C_N]\left(1 \leqslant N \leqslant \frac{n}{2}\right) \quad (C.2)$$

with

$$C_N = N(N - 1) \quad (C.3)$$

Substituting Eq. (C.3) into Eq. (C.2) gives:

$$M = 2N(n - N)\left(1 \leqslant N \leqslant \frac{n}{2}\right) \quad (C.4)$$

References

[1] Huang JS, Gibson LJ. Microstructural design of cellular materials—I: honeycomb beams and plates. Acta Metall Mater 1994;43(4):1643–50.
[2] Masters IG, Evans KE. Models for the elastic deformation of honeycombs. Compos Struct 1996;35(4):403–22.
[3] Gibson LJ, Ashby MF. Cellular solids, structures and properties. 2nd ed. Cambridge: Cambridge University Press; 1997.
[4] Wilson S. A new face of aerospace honeycomb. Mater Des 1990;11(6):323–6.
[5] Bitzer T. Honeycomb marine applications. J Reinf Plast Compos 1994;13(4):355–60.
[6] Thompson RW, Matthews FL. Load attachments for honeycomb panels in racing cars. Mater Des 1995;16(3):131–50.
[7] Price T, Timbrook RL. Structural honeycomb panel building system. Patent number US6, 253, 530 B1, July 3, 2001.
[8] Lu TJ. Heat transfer efficiency of metal honeycombs. Int J Heat Mass Transfer 1999;42(11):2031–40.
[9] Gu S, Lu TJ, Evans AG. On the design of two-dimensional cellular metals for combined heat dissipation and structural load capacity. Int J Heat Mass Transfer 2001;44(11):2163–75.
[10] Wen T, Tian J, Lu TJ, Queheillalt DT, Wadley HNG. Forced convection in metallic honeycomb structures. Int J Heat Mass Transfer 2006;49:3313–24.
[11] Hyun S, Torquato S. Optimal and manufacturable two-dimensional, Kagome-like cellular solids. J Mater Res 2002;17(1):137–44.
[12] Hashin Z, Shtrikman S. A variational approach to the theory of the effective magnetic permeability of multiphase materials. J Appl Phys 1962;33(10):3125–31.
[13] Hashin Z, Shtrikman S. A variational approach to the theory of the elastic behaviour of multiphase materials. J Mech Phys Solids 1963;11(2):127–40.
[14] Hayes AM, Wang A, Dempsey BM, McDowell DL. Mechanics of linear cellular alloys. Mech Mater 2004;36(8):691–713.
[15] Mohr D, Xue Z, Vaziri A. Quasi-static punch indentation of a honeycomb sandwich plate: experiments and modeling. J Mech Mater Struct 2006;1(3):581–604.
[16] Vaziri A, Hutchinson JW. Metal sandwich plates subject to intense air shocks. Int J Solids Struct 2007;44:2021–35.
[17] Vaziri A, Xue Z, Hutchinson JW. Performance and failure of metal sandwich plates subject to shock loading. J Mech Mater Struct 2007;2(10):1947–63.
[18] Ebrahimi H, Vaziri A. Metallic sandwich panels subjected to multiple intense shocks. Int J Solids Struct 2013;50:1164–76.
[19] Mori LF, Lee S, Xue ZY, Vaziri A, Queheillalt DT, Dharmasena KP, et al. Deformation and fracture modes of sandwich structures subjected to underwater impulsive loads. J Mech Mater Struct 2007;2(10):1981–2006.
[20] Wadley HNG, Dharmasena KP, Queheillalt DT, Chen Y, Dudt P, Knight D, et al. Dynamic compression of square honeycomb structures during underwater impulsive loading. J Mech Mater Struct 2007;2(10):2025–48.
[21] Babaee S, Jahromi BH, Ajdari A, Nayeb-Hashemi H, Vaziri A. Mechanical properties of open-cell rhombic dodecahedron cellular structures. Acta Mater 2012;60:2873–85.
[22] Xiong J, Ma L, Wu L, Wang B, Vaziri A. Fabrication and crushing behavior of low density carbon fiber composite pyramidal truss structures. Compos Struct 2010;92(11):2695–702.
[23] Xiong J, Ma L, Wu L, Liu J, Vaziri A. Mechanical behavior and failure of composite pyramidal truss core sandwich columns. Composites: Part B 2011;42:938–45.
[24] Xiong J, Vaziri A, Ma L, Papadopoulos J, Wu L. Compression and impact testing of two-layer composite pyramidal-core sandwich panels. Compos Struct 2012;94(2):793–801.
[25] Xiong J, Ma L, Pan S, Wu L, Papadopoulos J, Vaziri A. Shear and bending performance of carbon fiber composite sandwich panels with pyramidal truss cores. Acta Mater 2012;60:1455–66.
[26] Evans AG, Hutchinson JW, Fleck NA, Ashby MF, Wadley HNG. The topology design of multifunctional cellular metals. Prog Mater Sci 2001;46:309–27.
[27] Wadley HNG, Fleck NA, Evans AG. Fabrication and structural performance of periodic cellular metal sandwich structures. Compos Sci Technol 2003;63:2331–43.
[28] Wadley HNG. Multifunctional periodic cellular metals. Philos Trans R Soc A 2006;364:31–68.
[29] Wang AJ, McDowell DL. In-plane stiffness and yield strength of the periodic metal honeycombs. J Eng Mater Technol 2004;126(2):137–56.
[30] Fleck NA, Qiu X. The damage tolerance of elastic-brittle, two-dimensional isotropic lattices. J Mech Phys Solids 2007;55(3):562–88.
[31] Lakes R. Materials with structural hierarchy. Nature 1993;361:511–5.

[32] Pugno N. Mimicking nacre with super-nanotubes for producing optimized super-composites. Nanotechnology 2006;17(21):5480–4.

[33] Gao H. Application of fracture mechanics concepts to hierarchical biomechanics of bone and bone-like materials. Int J Fract 2006;138:101–37.

[34] Pugno N, Carpinteri A. Design of micro-nanoscale bio-inspired hierarchical materials. Philos Mag Lett 2008;88(6):397–405.

[35] Carpinteri A, Pugno N. Mechanics of hierarchical materials. Int J Fract 2008;150:221–6.

[36] Zhao Q, Kreplak L, Buehler MJ. Hierarchical structure controls nanomechanical properties of vimentin intermediate filaments. PLoS One 2009;4(10):e7294.

[37] Fratzl P, Weinkamer R. Nature's hierarchical materials. Prog Mater Sci 2007;52:1263–334.

[38] Pugno N, Chen Q. In plane elastic properties of hierarchical cellular solids. Eng Proc Phys Eng 2011;10:026–3031.

[39] Chen Q, Pugno N. Modeling the elastic anisotropy of woven hierarchical tissues. Compos Part B Eng 2011;42(7):2030–7.

[40] Chen Q, Huang S. Mechanical properties of a porous bioscaffold with hierarchy. Mater Lett 2013;95:89–92.

[41] Chen Q, Pugno NM. Bio-mimetic mechanisms of natural hierarchical materials: a review. J Mech Behav Biomed Mater 2013;19:3–33.

[42] Chen Q, Pugno N. Mechanics of hierarchical 3-D nanofoams. Europhys Lett 2012;97:26002.

[43] Chen Q, Pugno N. In-plane elastic buckling of hierarchical honeycomb materials. Eur J Mech A/Solids 2012;34:120–9.

[44] Chen Q, Pugno N. Competition between in-plane buckling and bending collapses in nano-honeycombs. Europhys Lett 2012;98:16005.

[45] Burgueno R, Quagliata MJ, Mohanty AK, Mehtad G, Drzale LT, Misraf M. Hierarchical cellular designs for load-bearing biocomposite beams and plates. Mater Sci Eng A 2005;390:178–87.

[46] Kooistra GW, Deshpande V, Wadley HNG. Hierarchical corrugated core sandwich panel concepts. J Appl Mech 2007;74(2):259–68.

[47] Fan HL, Jin FN, Fang DN. Mechanical properties of hierarchical cellular materials. Part I: Analysis. Compos Sci Technol 2008;68:3380–7.

[48] Garcia AP, Pugno N, Buehler MJ. Superductile, wavy silica nanostructures inspired by diatom algae. Adv Eng Mater 2011;13(10):B405–14.

[49] Taylor CM, Smith CW, Miller W, Evans KE. The Effects of hierarchy on the in-plane elastic properties of honeycombs. Int J Solids Struct 2011;48(9):1330–9.

[50] Ajdari A, Jahromi BH, Papadopoulos J, Nayeb-Hashemi H, Vaziri A. Hierarchical honeycombs with tailorable properties. Int J Solids Struct 2012;49:1413–9.

[51] Hyun S, Torquato S. Effective and transport properties of regular honeycombs for all densities. J Mater Res 2000;15(9):1985–93.

[52] Torquato S, Gibiansky LV, Silva MJ, Gibson LJ. Effective mechanical and transport properties of cellular solids. Int J Mech Sci 1998;40(1):71–82.

[53] Jasiuk I, Chen J, Thorpe MF. Elastic moduli of two dimensional materials with polygonal and elliptical holes. Appl Mech Rev 1994;47(1):S18–28.

[54] Wang Bo, Wang Bin, Cheng G. Multifunctional design of sandwich panels with Kagome-like cores. Acta Mater Compos Sinica 2007;24(3):109–15.